Characterization of the spectral signature of dual-fuel combustion luminosity: implications for evaluation of natural luminosity imaging

Aleš Srna, Rolf Bombach, Kai Herrmann, Gilles Bruneaux

Title

Characterization of the Spectral Signature of Dual-Fuel Combustion Luminosity: Implications for Evaluation of Natural Luminosity Imaging

Authors:

- **Aleš Srna,** Paul Scherrer Institute, OVGA 119A, CH-5232 Villigen PSI, Switzerland
  - Email: ales.srna@psi.ch; Tel.: +41 79 310 87 74, Fax: +41 56 310 26 24
- **Rolf Bombach,** Paul Scherrer Institute, OVGA 107, CH-5232 Villigen PSI, Switzerland
- **Kai Herrmann,** Institute of Thermal and Fluid Engineering, School of Engineering, University of Applied Sciences Northwestern Switzerland, Klosterzelgstrasse 2, CH-5210 Windisch, Switzerland
- **Gilles Bruneaux**, IFP Energies nouvelles, 1 et 4 avenue de Bois Préau, 92852 Rueil-Malmaison, France; Institut Carnot IFPEN Transports Energie

Abstract

N-dodecane pilot-ignited lean-premixed natural-gas combustion has been investigated in a rapid compression-expansion machine. The aim of this study was to characterize the combustion spectral footprint: identify the main sources of natural luminosity, characterize the temporal brightness evolution, and provide guidance for the evaluation of natural luminosity imaging acquisitions. Natural luminosity spectra in the range of 280 – 610 nm were acquired, 1D-resolved along the injector axis, using an imaging spectrograph and intensified high-speed camera. Four significant contributions to the natural luminosity were identified: Soot, OH* and CH* chemiluminescence, as well as overlapping broadband chemiluminescence of CO_2*, CHO* and CH_2O* species. The CH* chemiluminescence could be only detected at ignition and during the pilot-fuel combustion period. Similarly, initial OH* and broadband luminosity were also detected at ignition. However, this luminosity additionally increased late in the cycle, when methane, enriched with diluted pilot-fuel, forms an extensive burnt zone with close-to-stoichiometry conditions. For the ignition delay detection, imaging of broadband luminosity has to be recommended since at ignition it shows a higher rise-rate than the OH* chemiluminescence. It was shown that, after ignition, in dual-fuel combustion, the coupling between the natural luminosity and heat release-rate is too weak to extract useful information.

1 Introduction

The optical investigations of combustion often rely on the imaging of flame natural luminosity. Such detection is state of the art and utilizes flame imaging in various wavelength ranges: around 310 nm for OH* chemiluminescence detection, around 430 nm for the detection of CH*, or broadband/color imaging for the detection of all luminescent species in the flame. Nevertheless, the chemiluminescence of all species in flames strongly depends on the temperature, reaction rates, equivalence ratio, pressure as well as the strain rate. Furthermore, such imaging is prone to the interference by soot incandescence. When combustion processes are investigated optically, a study of the spectral signature of combustion is of high value to identify possible interferences as well as to establish a framework for the interpretation of results. During the validation of CFD studies often CH* or OH* chemical mechanisms are used to predict the chemiluminescence signal. For comparison with experiments, it is of paramount importance that the experiments indeed detect only the target species emission.

The natural flame luminosity originates from the emission of several species emitting in a wide range of wavelengths. In spark-ignited premixed-combustion engines, several studies investigated the flame and spark-plasma spectra [1]. Within the variety of combustion concepts featuring auto-ignition, the spectral footprint of non-sooting Homogeneous-Charge Compression-Ignition (HCCI) is most thoroughly investigated. In the visible range, studies report broadband chemiluminescence between 300 nm – 600 nm to be the primary emission source [2-6]. Additionally, the chemiluminescence of CH* and OH* becomes visible at sufficiently high equivalence ratio [4,5]. The ratio of CH*/OH* as well as the intensity of the broadband (BB) luminosity, were shown to correlate well with the local equivalence ratio, and both, the OH* and BB signals were found to be proportional to the Heat Release Rate (HRR) [2]. With increasing level of spatial mixture stratification, the combustion regime

changes to partially premixed combustion until the conventional diesel combustion regime is reached. At diffusion combustion stage, soot becomes the dominant source of luminosity at longer wavelengths [2,7-9]. Nevertheless, at shorter wavelengths, a considerable portion of luminosity still originates from OH*, CH* and BB luminosity. During the autoignition and premixed burning part, BB contributions from both, CO_2* as well as CH_2O* and CHO* chemiluminescence were identified, while at later stages the BB luminosity is again dominated by CO_2* [7,8]. The proportionality of HRR and OH*/BB intensity does not apply anymore.

The chemical mechanisms describing the formation of the excited luminescing species can aid the understanding of the experimentally observed trends. A short review of the literature suggests the different chemiluminescent species to be produced at different reaction stages during the combustion. First, excited CH*, originating from the oxidation reactions of two-carbon-atom species, is expected to form [10,11]. Therefore, considerably stronger CH* chemiluminescence in flames of higher hydrocarbons is expected relative to methane. Next, CH_2O and CHO species will be formed. Literature investigating these particular species chemiluminescence is scarce. CH_2O* is suggested to be formed in the recombination reactions of 1-carbon atom radicals [12,13] and CHO* during the oxidation reactions of CH_2O with the OH radical [13,12]. At last, the formation of CO_2* and OH* species is expected. CO_2* is formed mostly through the oxidation of CO with O atoms, while the OH* originates from the recombination reactions of H and O atoms as well as from the oxidation of CH radical with O_2 [13,14,10,15]. Contrary to CH*, CHO*, and CH_2O*, which are abundant only during the combustion, the CO+O→CO_2* and O+H→OH* reactions remain active also in the hot burnt zones with close to stoichiometric conditions [13,14]. This leads to a persistent CO_2* and OH* luminosity also in the burnt regions.

The dual-fuel combustion process comprises of pilot-fuel auto-ignition in methane/air mixture, followed by turbulent premixed flame propagation through the remaining charge. The fuel equivalence ratio, as well as the ratio of premixed fuel and pilot-fuel, is strongly stratified in the combustion chamber. Several optical studies investigated this combustion using chemiluminescence and schlieren imaging [16-21]. The common observation is that methane strongly defers the ignition delay, and during the pilot-fuel combustion a higher HRR is observed due to the simultaneous combustion of premixed methane.

The motivation for this study was the observation of a decoupled evolution of HRR and OH* brightness, perceived in our previous work [16,17] and other studies [19]. Figure 1 illustrates the combustion HRR rate compared to the field-of-view integrated OH* chemiluminescence for a sweep of background methane equivalence ratios in the RCEM [16]. Adding methane into the charge air leads to an increased peak HRR (by a factor up to 2) relative to the pilot-fuel-only case. The OH* chemiluminescence signal appears to be decoupled from the HRR. In dual-fuel cases, the highest OH* chemiluminescence signal has been detected during the premixed flame propagation stage (1-2 ms after ignition) and up to 10 times higher OH* signals were observed for higher methane background concentrations. This behavior has also been reported by Schlatter et al. [19] for *n*-heptane pilot fuel. Up to date, it was not investigated whether this signal originates from OH*, BB chemiluminescence or possibly soot black-body radiation.

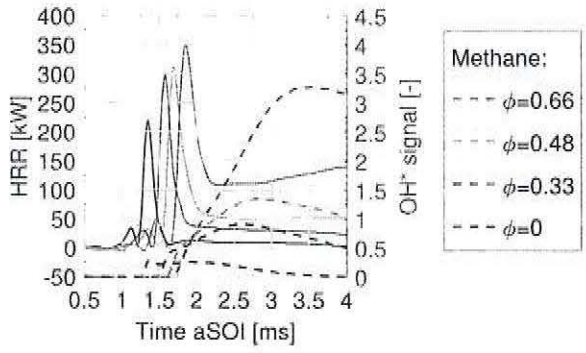

Figure 1: Combustion HRR (full-line) and field-of-view integrated OH* imaging signal (dashed) for a variation of premixed methane equivalence ratio, acquired using the test setup from [16]. Conditions: T_{SOI} = 810 K, p_{SOI} = 25 bar, injection duration: 0.58 ms, injection pressure: 600 bar, pilot-fuel: *n*-dodecane.

Figure 1 indicates a considerably slower rise rate of OH* signal at ignition in dual-fuel cases. This dependence of the intensity and temporal evolution of the OH* chemiluminescence might have a strong implication on the detection of ignition delay using a thresholding approach. Similar might also apply for the general natural luminosity imaging. The correlation between the local ignition and chemiluminescence is presented in Figure 2 by comparing the simultaneously acquired schlieren and OH* images from diesel and dual-fuel case with the same ignition delay. The optical system sensitivity was unchanged [17]. At ignition, the first OH* signal is expected to be detected. The temporal evolution of the Schlieren signal is more complex [22]: in the diesel case, first schlieren signals with high contrast are detected in the fuel-vapor zones due to the evaporative cooling. The low-temperature combustion generated heat compensates for the evaporative cooling and leads to a softening of the schlieren signal, which then reappears after ignition.

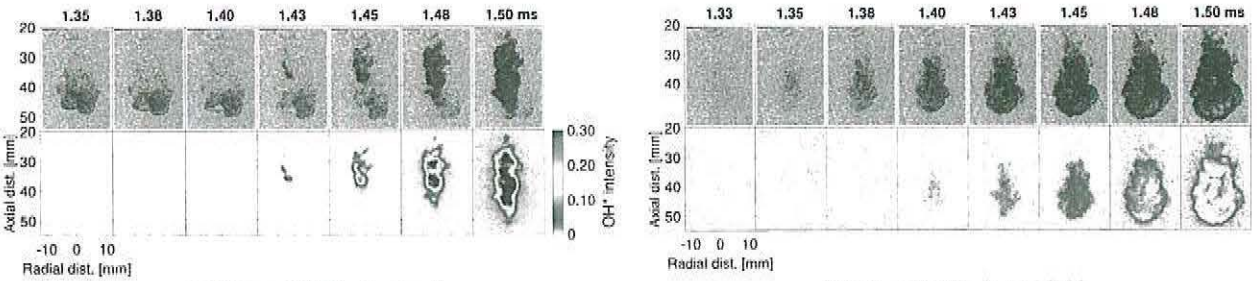

(a) T_{SOI} = 770 K, ϕ_{CH4} = 0 (b) T_{SOI} = 850 K, ϕ_{CH4} = 0.66

Figure 2: Time-series of schlieren and OH* chemiluminescence images for (a) diesel, and (b) dual-fuel case with approximately the same ignition delay.

In the diesel case (Figure 2a), the first appearance of the OH* signal (1.06 ms) correlates well with the first schlieren signal reappearance upstream of the spray tip. The OH* intensity quickly rises and exceeds 30% of the camera dynamic-range already 50 µs after ignition. In contrast, the dual-fuel case shows a very slow rise of OH* signal. First photons are visible on the OH* images at 1.02 ms after the start of injection. It takes more than 125 µs to reach the intensity comparable to 30% of the camera dynamic-range used in the diesel case. Schlieren imaging is more sensitive to detect ignition in the dual-fuel case – the first schlieren signal reappears already 1-2 image frames prior to the first OH* photons being detected (0.99 ms) This is considerably earlier than the ignition delay (1.06 ms) detected by the common thresholding technique used in [16]. Depending on the sensitivity of the employed detection system, the slow rise rate of the OH* signal can lead to significant overprediction of the ignition delay, as reported in [19].

Observing the peculiarity of ignition detection in dual-fuel cases, the objectives of the present investigations were: (1) characterize the dual-fuel combustion natural luminosity relative to the luminosity of conventional diesel combustion, (2) identify the species contributions to the natural luminosity, (3) explain the observed temporal evolution of OH* signal intensity, and (4) provide guidelines for the evaluation of dual-fuel natural luminosity imaging.

This publication is structured as follows: First, the experimental test rig, the 1D-spectroscopy setup for the time-resolved acquisition of flame-luminosity spectra, as well as the processing approach, are presented. In the results section, the species contributing to the natural luminosity were identified, and the dependence of spectral emission on the charge and injection conditions is presented. The discussion focuses on the implications of the observed luminosity trends for the evaluation of natural luminosity imaging in the dual-fuel combustion investigations.

2 Experimental Apparatus

2.1 *Rapid Compression-Expansion Machine (RCEM)*

The Rapid Compression Expansion Machine (RCEM) used in this study is a free-floating piston machine with a bore of 84 mm and stroke of up to 249 mm. Methane-air mixture is conditioned in the combustion chamber prior to the rapid compression, and the mixture is ignited with a pilot injection initiated when the combustion chamber pressure reaches the set

threshold level (p_{SOI}). To admit the pilot fuel, a single-hole coaxial diesel injector with a 100 µm conical nozzle is used, mounted at the cylinder periphery, with the injector axis in the radial direction relative to the RCEM cylinder axis. Readers interested in the detailed information on the RCEM combustion chamber geometry are referred to [17]. The detailed description of the RCEM operation principle and strategy are available in [23].

2.2 *Experimental conditions*

In this study, the RCEM has been operated at the maximal BDC displacement setting (1.38 dm^3 displacement, 249 mm BDC clearance to the cylinder head) to have a sufficient TDC clearance for minimizing the pilot spray interaction with walls. The operation strategy of the RCEM was selected based on previous operation experience to assure high-repeatability of the conditions at Start Of Injection (SOI): A mixture of methane and air with a BDC pressure of 1.2 bar has been conditioned in the cylinder before the rapid compression to assure homogeneous mixture [17]. The machine was operated at a compression ratio of about 20, and the pilot fuel injected early in the cycle (ca. 3.5 ms before TDC) when the cylinder pressure reached a threshold of 25 bar. The bulk charge temperature at ignition was controlled by adapting the cylinder head and walls temperature at the BDC. Consequently, the BDC charge temperature (equal to the wall temperature [24]) and the temperature at the SOI (T_{SOI}) were changed.

The measurement matrix consisted of four main variations: Variation of the premixed methane equivalence ratio (ϕ_{CH4}) in the range between $0-0.66$, variation of T_{SOI} (770 K, 810 K, 850 K), variation of pilot injection duration (0.38 ms, 0.58 ms, 1.21 ms) as well as the charge oxygen content (15%, achieved by dilution of air with nitrogen.). The injection pressure was kept constant at 600 bar (steady fuel injection rate: 2.43 mg/ms). Table 1 summarizes the experimental matrix and conditions of this study.

Table 1: Overview of the experimental matrix. Values in braces were not acquired for all cross-variations. The values of the standard case are printed bold.

	T_{SOI} and ϕ_{CH4} variation	Injection duration variation	Charge oxygen variation
Charge BDC pressure	**1.20 bar**		
Stroke	**236.5 mm ± 1 mm**		
Compression ratio	**20**		
BDC temperature	343 K, **363 K**, 383 K	**363 K**	
Pressure at SOI	**25 bar**		
Temperature at SOI (T_{SOI})	770 K, **810 K**, 850 K	**810 K**	
Charge oxygen content	**21%**		15%
Premixed methane equivalence ratio (ϕ_{CH4})	0, 0.33, (0.48), (0.53), 0.59, (0.66)	0, 0.33, 0.59	0, 0.33, 0.59 (relative to 21% oxygen)
Pilot injection duration	**0.58 ms**	0.38 ms, **0.58 ms**, 1.21 ms	**0.58 ms**
Pilot-fuel mass per injection	**1.18 mg**	0.64 mg, **1.18 mg**, 2.67 mg	**1.18 mg**
Pilot injector energizing time (ET)	**400 µs**	300 µs, **400 µs**, 700 µs	**400 µs**
Pilot injection pressure	**600 bar**		

2.3 *Optical setup*

Two different sets of optical diagnostics were used in this study. The introduction figures and Figure 9 present results acquired with a simultaneous Schlieren and OH* chemiluminescence imaging setup described in [17]. Since both techniques represent state of the art, they are not further introduced here. Second, the combustion spectral footprint was characterized with a 1D-spectroscopy setup described below.

Figure 3 presents the 1D-spectroscopy setup employed to investigate combustion luminosity spectra. Emission was acquired through the piston window over two UV aluminum mirrors. A part of emitted light was reflected by the dichroic beamsplitter

towards the spectrograph and projected on the spectrograph slit using an UV objective (Sodern Cerco 94 mm f/4.1). The application of an imaging spectrograph (Acton SP-300i, grating 300 lines per mm, blazed for 500 nm) enabled 1D resolution of the spectrum along the slit. The spectrally dispersed light was detected with an intensified high-speed camera system (LaVision HS-IRO coupled with Photron FastCam SA1.1) operated at a frame rate of 20 kHz (intensifier gate 45 µs). A slit with of 100 µm was used, reduced to 40 µm for strongly sooting cases, and the intensifier gain was adapted between 7 – 20 counts/photoelectron depending on the flame brightness to fully exploit the camera dynamic-range. The wavelength range between 250 – 600 nm was acquired. Below 300 nm only weak radiation was detected, and therefore, separation of different grating orders was not necessary. The spectral resolution of about 2 nm and the resolution along the slit of about 1 mm were limited by the spectrograph aberrations and not by the camera resolution. The field of view of the 1D spectroscopy was set to spectrally resolve the flame emission and soot luminosity in one dimension along the pilot-injector axis.

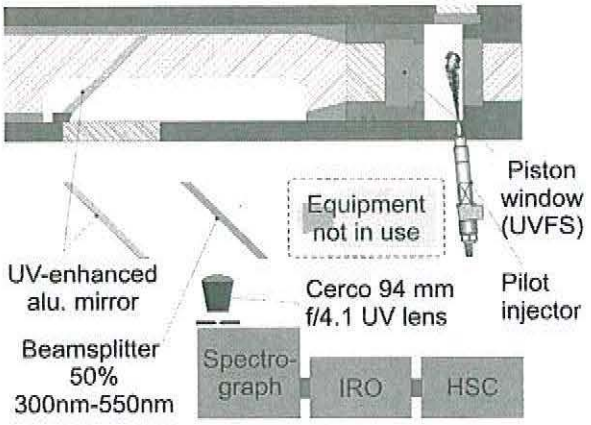

Figure 3: Optical setup for 1D-spectroscopy acquisitions at the RCEM. A rough sketch of the RCEM geometry and optical access is shown as well.

2.4 *Spectra processing*

Spectral images were processed to extract the spectra and identify the contributing species. First, the images were averaged over 10 experimental repetitions, and across 10 pixels along the axial direction (corresponding to 2 mm). The so obtained raw spectra were further processed as demonstrated in Figure 4.

The raw spectra were corrected for the system spectral and spatial dependence of transmission and quantum efficiency (more detailed description in [17]). In the next stage, the presence of soot incandescence has been detected (Figure 4 (a) sooting combustion, (b) non-sooting combustion). For this purpose, a soot-emissivity corrected Planck's law curve is fitted to the corrected spectrum in the wavelength range of 470 – 585 nm. The soot emissivity relation proposed by Musculus [25] has been used. In this spectral range, the contribution of flame chemiluminescence to the overall intensity is expected to be smallest in the available spectral range. The result of fitting procedure is a value of the apparent soot temperature at the spectrum spatial location, and the estimated brightness of soot incandescence over the complete wavelength range investigated here. The blue dashed curve in Figure 4a demonstrates the resulting Planck's law curve fit. Two criteria were devised to distinguish sooting combustion from non-sooting cases based on the Planck's law fit results. The first criterion proves the apparent soot temperature for unreasonable values: if the apparent temperature lies outside the 1500 – 2800 K range the emission was assumed not to originate from soot incandescence, therefore, the case was deemed non-sooting. The second criteria required that soot incandescence considerably contributes to the total flame luminosity at shorter wavelengths (450 nm): The Planck-fitted soot incandescence brightness at 450 nm (blue dashed line Figure 4a) was compared to the total emission at 450 nm (black line Figure 4a). Cases, where soot incandescence did not exceed an arbitrary threshold of 50% of the total emission, were assumed to be non-sooting. These criteria were deemed to reliably determine sooting combustion by analysis of spectra with the naked eye: it was straightforward to distinguish sooting combustion spectral features from the non-sooting.

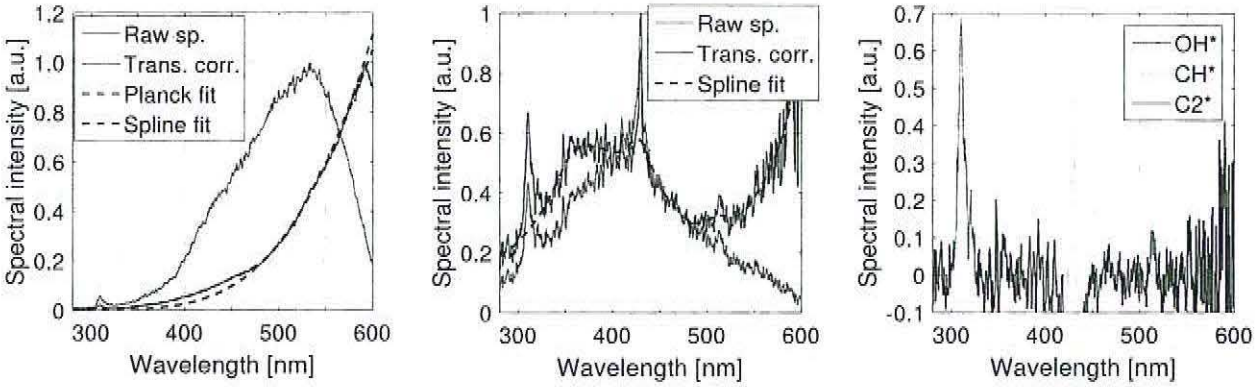

(a) Spectrum of a mildly sooting case (b) Non-sooting case spectrum (c) Subtracted BB luminosity

Figure 4: 1D-spectroscopy processing approach: (a) The raw spectrum (sp.) and transmission corrected (Trans. corr.) spectrum of a sooting combustion event, with demonstrated Plank and spline-fit curves. (b) Raw spectrum and transmission corrected spectrum of a non-sooting combustion event, with a demonstrated spline-fit result. (c) The spectrum from (b) with subtracted broadband luminosity.

In the sooting cases, the fitted incandescence luminosity was subtracted from the spectra. In non-sooting cases, this processing step was skipped. The remaining signal can be attributed to the flame natural luminosity. Flame luminosity (Figure 4a) shows well distinct peaks at around 310 nm, 430 nm, and 510 nm on a pedestal of broadband luminosity. The separation of the OH*, CH* and C_2* chemiluminescence from the broadband (BB) luminosity follows the approach proposed in [2]. A spline fit with a long kernel (MATLAB function 'fit' using the 'SmoothingSpline' functionality with the smoothing parameter set to 0.001) has been used to approximate the spectrum of the background luminosity – whereas the points from the bands 305 – 320 nm, 423 – 439 nm, and 510 – 520 nm were not given to the fit function. In this way the broadband luminosity at wavelengths with overlapping narrowband species chemiluminescence was approximated. In the second step, the spline-approximated broadband luminosity has been subtracted from the spectrum (Figure 4b). The integrated signal in the spectral band of 325 – 350 nm has been used as a measure for broadband luminosity intensity. The selection of this spectra range was motivated by minimizing the interference from possible soot luminosity. The intensity of the remaining peaks (after the spline-fit subtraction) in the range of 305 –320 nm, 423 – 439 nm, and 510 – 520 nm has been integrated over the corresponding bands and assigned as the intensity of OH*, CH* and C_2* chemiluminescence, respectively (Figure 4b). However, the C_2* chemiluminescence was too weak to be detected reliably and was not further processed.

In sooting cases, this method cannot distinguish between the soot black-body luminosity and the broadband luminosity in the upper wavelength range (above 450 nm). This results in an underestimation of the broadband luminosity in sooting cases since all light emission in the range of 470 – 590 nm is considered to originate from the blackbody luminosity. In the shorter wavelength range used for broadband luminosity estimation (325 – 350 nm) this error is substantially smaller (estimates less than 20% in the most sooting considered cases) and is not expected to influence the interpretation of the results in this work.

3 Results

3.1 *Temporal evolution of the flame emission spectra*

The temporal evolution of the spectral emission of a non-sooting diesel ($\phi_{CH4} = 0$) and non-sooting dual-fuel ($\phi_{CH4} = 0.66$) combustion case at $T_{SOI} = 810$ K is presented in Figure 5. In both cases, at the time of ignition, luminosity is detected across the complete spectral range acquired here. Besides the OH* chemiluminescence emission in the range of 305 – 320 nm also two bands of broadband luminosity are visible: A band extending from approximately 300 – 500 nm, and a band extending from 500 nm towards longer wavelengths. In accordance with the literature, the emission in the first band was attributed to CO_2*, CHO*, and CH_2O* emissions. The emission of the second band persists longer than the broadband (BB) and OH* luminosity. In the literature this emission is commonly attributed to the overlapping H_2O vibration-rotation bands 500 –

580 nm, and the NO-O continuum 400 – 800 nm [26]. In some of the dual-fuel cycles (c.f. Figure 5b) at a later stage, an additional emission at 589 nm was detected and attributed to sodium D-line emission. The sodium is believed to originate from the lubrication agent used in RCEM.

The emission of CH* (430 nm) is short-lived and was only detected in the very early phase of combustion –faintly visible for the diesel case in Figure 5a inlay. The emission of CH* in the diesel case is also accompanied with a bright emission in the wavelength band from 300 – 450 nm. Contrary to the light emitted late in the cycle, during this transient the emission in blue wavelengths is brighter than at wavelengths longer than 500 nm. In accordance to [7,8] authors attributed this to the light emitted from CH_2O* and CHO*, which are not expected to be formed after the pilot fuel is consumed. Therefore, the emission later in the cycle might be primarily due to CO_2*. However, no spectral features could be detected to confirm this assumption.

A very large difference in the brightness of the diesel and dual-fuel case required different color scale representation: diesel case was multiplied by a factor of 10. The bright transient luminosity at ignition seen in the diesel case was not visible in the dual-fuel case (Figure 5b). At late stages of combustion no significant difference in the spectral footprint of the cases in Figure 5 is apparent. In the following, the analysis focuses on the dependence of OH*, CH*, and broadband emission (BB) on the methane equivalence ratio, charge temperature, and pilot injection duration.

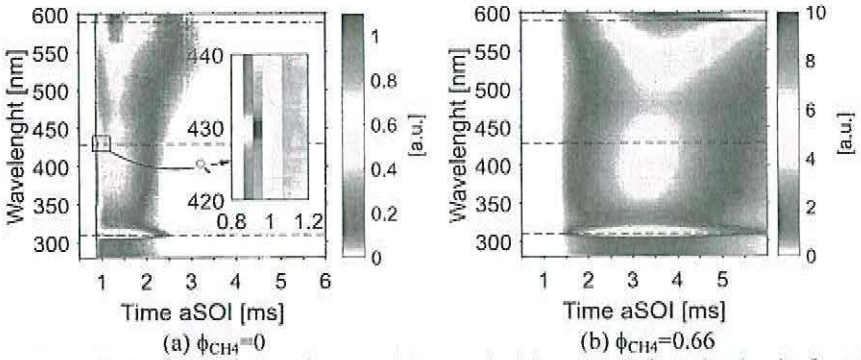

Figure 5: Temporal evolution of averaged (across the injector axis) flame luminosity for (a) diesel, and (b) dual-fuel case. Conditions: T_{SOI} = 810 K, ET = 400 µs. The brightness of the diesel case is multiplied by a factor of 10 to utilize the complete range of color representation. In the diesel case (a) the inlay plot shows magnified the spectral band around 430 nm at a time around ignition.

The spatially 1D-resolved temporal evolution of the combustion spectral intensity of BB, OH* and CH* chemiluminescence along the injector axis for a variation of methane equivalence ratio is presented in Figure 6. A comparison of the OH* and BB chemiluminescence intensity shows only minor differences between the spatial signal distribution of both species. Only during the pilot-fuel combustion a difference between the OH* and broadband chemiluminescence evolution was observed – the broadband signal peaks and shows a higher intensity than the OH* signal.

The signal of CH* shows a considerably different behavior than the OH* and BB. It is only present early in combustion and not detectable during the premixed flame propagation phase. It shows a high rise-rate at ignition and thus aids the detection of ignition delay. In the late phase of combustion, CH* intensity is very weak, overlaid with bright BB luminosity signal. This behavior is in agreement with the literature suggesting that the CH* is formed during the oxidation of C_2 and C_2H species. In the combustion of long hydrocarbon pilot-fuel and premixed methane, considerably more C_2 is expected during the combustion of pilot fuel.

The different rise rates of species chemiluminescence at ignition will have a strong influence on the measured ignition delay using a thresholding technique (as already observed in Figure 2). This is demonstrated by the dashed vertical lines in Figure 6. When detecting the ignition based on an OH* imaging thresholding approach, the slow OH signal rise rate at ignition might lead to an imprecise ignition delay detection, depending on the system sensitivity and the selected threshold level. This might be especially critical in dual-fuel cases where a very slow rise of the OH* signal after the ignition has been observed. On the

other hand, CH* and BB signals show a faster rise rate at ignition and appear to enable a more precise ignition delay detection. This will be further assessed in the discussion section.

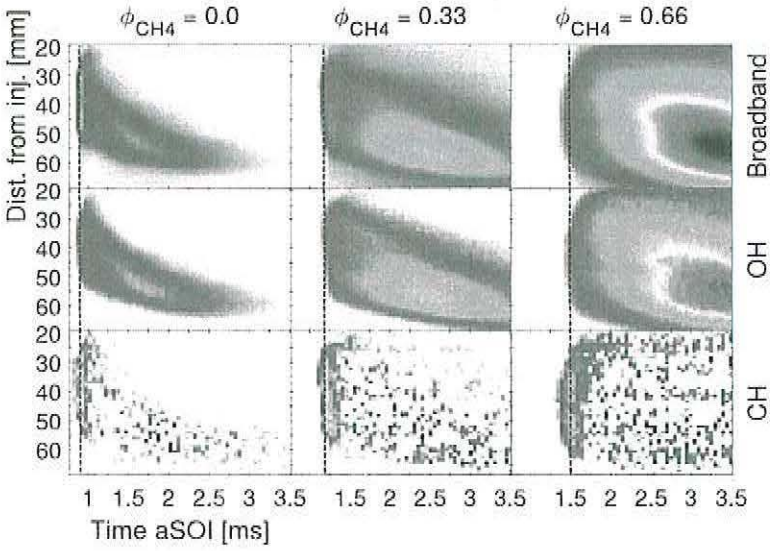

Figure 6: Temporally and spatially resolved intensity of the broadband, OH*, and CH* chemiluminescence for a variation of the background methane equivalence ratio. Conditions: T_{SOI} = 810 K. Pilot injection: ET = 400 µs. Injection from top to bottom.

Figure 7 extends the analysis of the temporal species chemiluminescence evolution to a variation of charge and pilot-injection conditions. The evolution of CH*, OH*, and BB-chemiluminescence intensities for an extensive variation of background methane equivalence ratio, charge temperature, injection duration, and simulated exhaust gas recirculation (EGR) is presented.

The duration of CH* emission moderately increases with the addition of methane into the background mixture. This implies a prolonged duration of the pilot-fuel burning. However, the injection duration does not show a significant influence on the duration of CH* signal. This also applies to ϕ_{CH4} = 0 cases with reduced charge oxygen content (bottom row, Figure 7), while to the contrary, a combination of reduced oxygen and methane addition considerably increases the duration of the CH* emission, indicating prolonged pilot-fuel combustion.

For all variation of conditions in this study, a considerable increase of OH* signal with the addition of methane has been observed. Focusing first on the ϕ_{CH4} variation at T_{SOI} = 810 K and ET = 400 µs (upper row), the diesel case shows a fast rise of OH* signal at ignition, followed by a plateau for 1 ms and consequent signal decrease. With increasing ϕ_{CH4}, the OH* signal rises later (longer ID) and shows lower rise rates. Nevertheless, following the initial faster rise, the signal keeps slowly rising for 1-3 ms depending on the ϕ_{CH4} and drops considerably later. As already observed above, a several times higher peak emission of OH* is detected with increasing ϕ_{CH4}. This influence is especially pronounced under the T_{SOI} = 770 K conditions and for short injections. For those lower T_{SOI} cases (Figure 7, 2nd row), with ϕ_{CH4} = 0, the maximal equivalence ratio of pilot fuel rapidly leans-out, leading to a rapid decrease of OH* brightness. With the addition of methane, the methane and pilot-fuel combination form long persisting zones with close to stoichiometric conditions. This is aligned with the longer persistence of the high OH* signal observed in the spectral footprint.

At late stages after ignition, OH* and BB signals show a very similar temporal evolution as already observed in Figure 6. This applies to all variations in this study. Nevertheless, significant differences between the brightness of OH* and BB were detected during the pilot-fuel burning period, with a steeper rise of BB emission at ignition. These results suggest BB chemiluminescence to be a better marker of the HRR during the pilot-combustion phase than the OH* signal. The differences in the rise rate become pronounced at higher ϕ_{CH4} concentrations.

In case of reduced charge-oxygen-concentration, a substantial reduction of all chemiluminescence intensities has been observed. For 15% O_2, in comparison to 21% O_2 at T_{SOI} = 770 K (similar ignition delays), about two times lower CH* intensity has been observed. OH* and broadband luminosity are even more influenced: about a factor 4 lower OH*, and factor of 2 lower BB signals were observed in the diesel-case. With the addition of methane at 15% O_2, the peak OH*, and BB luminosity do not increase like for 21% O_2. Therefore, at ϕ_{CH4} = 0.59, going from 15% O_2 to 21% O_2, the flame brightness for both, OH* and BB chemiluminescence increases by a factor of about 30. This was attributed to the decreased adiabatic flame temperature at reduced charge oxygen content.

Often reported correlations of CH*, or CH*/OH* ratio, to the combustion equivalence ratio obviously do not apply in these cases. Moreover, no correlation of the cumulative CH* emission to the total pilot-fuel quantity has been observed. On the other hand, the peak CH* intensity seems to increase with rising T_{SOI}, and slightly decreases with higher methane content: up to 30% of CH* signal decrease was observed with a methane concentration of ϕ_{CH4} = 0.66. This complex dependence of CH* luminosity on the charge parameters renders any quantification based on CH* impossible.

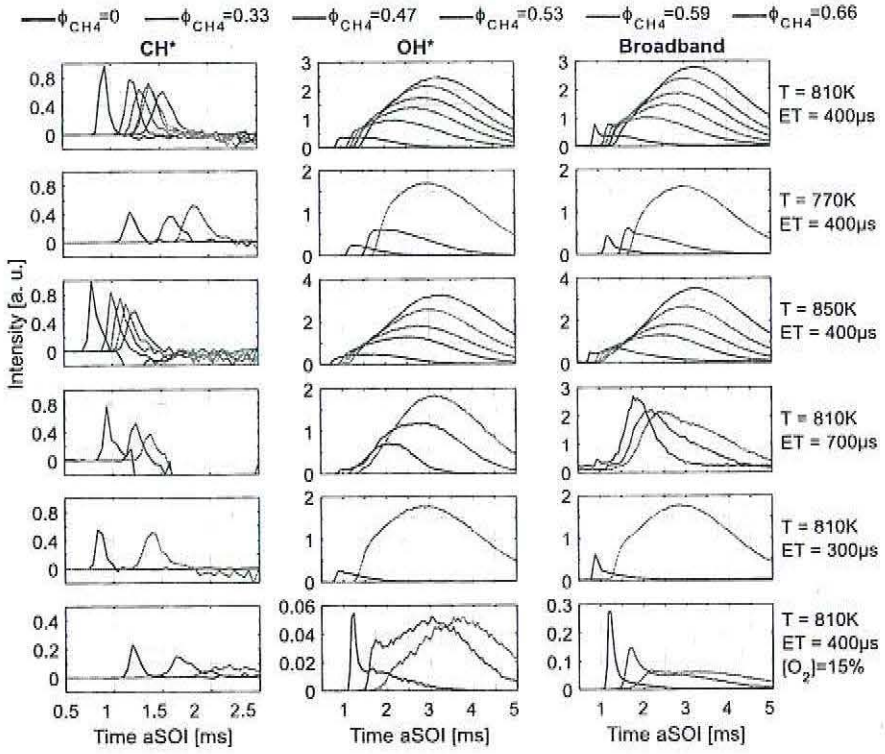

Figure 7: Evolution of CH*, OH*, and BB luminosity for a variation of ϕ_{CH4}, T_{SOI}, injection ET and charge oxygen content. Line color marks the ϕ_{CH4}.

4 Discussion

The discussion section focuses primarily on the implications of the observed spectral features for the evaluation of dual-fuel combustion natural luminosity imaging. It has been already established in the results section that the measurement of BB signal is, in general, more reliable to detect ignition than OH*, due to the steeper rise rate of BB signal at ignition. Furthermore, the BB emission spectra overlap with the emission bands of OH* and CH*. Therefore, conventional bandpass filter imaging of OH* and CH* might primarily detect BB luminosity instead of the targeted species.

Figure 8 presents the temporal evolution of the percentage of OH* and CH* contribution to the overall signal passing a bandpass filter for corresponding species detection. The heat release rate (HRR, bottom axes) is plotted for reference. This processing follows the analysis proposed by Najafabadi et al. [2]: ideal OH* and CH* bandpass filters transmitting in the wavelength bands of 305 – 320 nm and 425 – 435 nm were assumed for OH* and CH*, respectively. The portion of the luminosity originating from BB chemiluminescence was separated from the narrow-band OH* and CH* emission based on spline fitting (section 2.4).

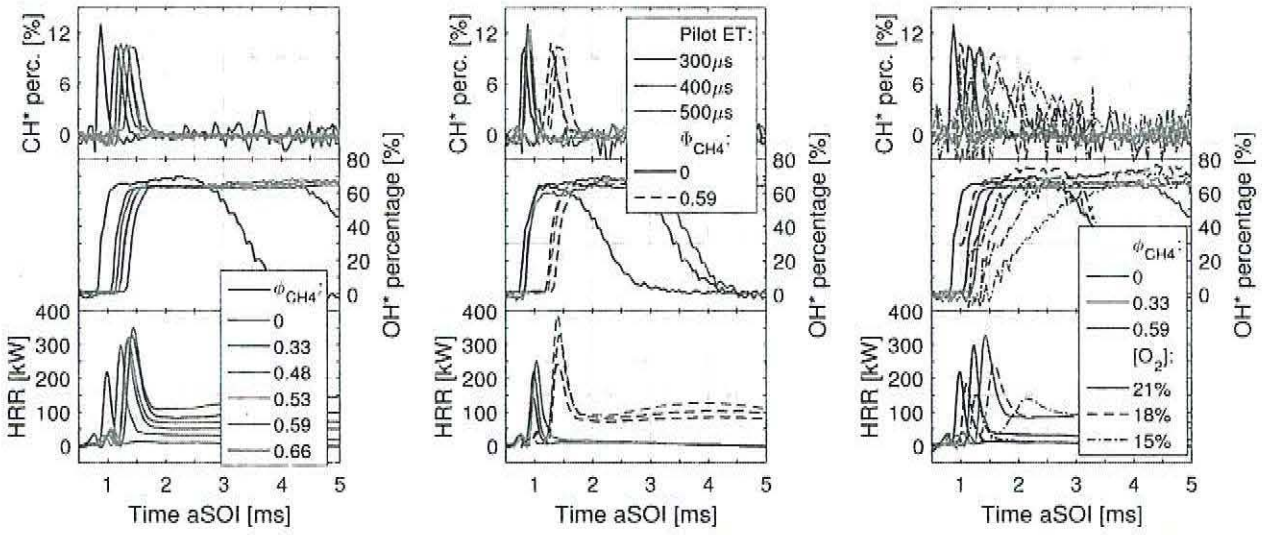

(a) ϕ_{CH4} variation, ET = 400 μs (b) ϕ_{CH4} and ET variation (c) ϕ_{CH4} and EGR variation

Figure 8: Temporal evolution of the contribution of the narrow-band CH* (upper axes), and OH* (middle axes) chemiluminescence to the overall luminosity emitted in the spectral bands used for OH* and CH* chemiluminescence detection. The HRR (bottom axes) is plotted for reference. Variations: (a) ϕ_{CH4} variation, (b) ϕ_{CH4} and ET variation, and (c) ϕ_{CH4} and EGR variation.

In the literature a strong dependence of the CH* and OH* contribution on the level of premixed-ness in partially-premixed compression ignition combustion was observed [2]: only BB luminosity (no OH* or CH*) was observed for fully premixed combustion of heptane (ϕ up to approximately 0.40). In [2], for conditions with higher mixture stratification leading to a considerable portion of diffusion combustion, narrow-band species luminosity contributing up to 50% for OH*, and up to 15% for CH*, in the corresponding wavelength bands, were reported. Indeed, similar maximum values of the narrow-band species contributions were observed in the present study – peak values in the range of 60-70% OH* contribution and 10-13% CH* contribution were observed for all investigated conditions. This is expected since the dual-fuel combustion exhibits a considerable level of mixing inhomogeneity and higher equivalence ratios than investigated in [2].

It is interesting to compare the temporal evolution of the narrowband chemiluminescence contribution to the filtered signal. Analyzing the ϕ_{CH4} variation (Figure 8), a good agreement of the CH* contribution with peak HRR is observed: the fast rise of CH* portion at ignition and disappearance of the signal after the pilot-fuel is consumed during the peak HRR. This is in agreement with the conclusion that CH* emission only occurs during the pilot-fuel combustion. On the contrary, the portion of OH* starts to increase after ignition and reaches a steady level of about 65% only after the pilot-fuel is consumed. This level of OH* contribution remains at a plateau level for several milliseconds after the peak HRR and begins to decrease very late in the cycle when the total flame brightness rapidly decreases.

The temporal evolution of species contribution to luminosity was found mostly insensitive to injection duration and therefore insensitive to the pilot-fuel mixture fraction at ignition (Figure 8b). Despite the four times larger fuel mass in case of the longest injection, maximal CH* contribution remains constant at about 12% of all luminosity in the 430 nm band. The same was also observed in the dual-fuel case (dashed lines, different ETs). Nevertheless, a slightly lower peak CH* contribution of

10% was reached. Similarly, also OH* again rises to a plateau value of 65% which is reached after the pilot-fuel is burnt. The contribution of OH* starts to deviate from this plateau only late in the cycle when the mixture considerably leans out.

A more substantial dependence of CH* and OH* contributions on ϕ_{CH4} was observed only in those cases with reduced charge oxygen concentration (Figure 8c). Reduced peak CH* contributions were observed at lower charge O_2 (dashed and dot-dashed lines) as well as with increasing ϕ_{CH4}. This is most probably due to slower pilot-fuel combustion (implied by longer CH* signal persistence) leading to a simultaneous luminosity of already burnt and burning pilot-fuel zones. In addition, the evolution of OH* contribution appears to be dependent on pilot-fuel burning duration. For all O_2 contents, the same plateau level of OH* contribution is achieved – however, considerably later for lower charge O_2, corresponding to the time when CH* contribution decreases.

Overall, this analysis confirms the implications for natural-luminosity imaging evaluation stated above. At ignition, the BB luminosity mostly dominates the signal in OH* spectral range. Therefore, the acquisition of BB luminosity is preferred for the detection of ignition. This influence has to be accounted particularly also for validation CFD simulations employing an OH* chemiluminescence chemical mechanism – during the pilot-fuel burning considerable differences to the experimental data might be observed since before the pilot-fuel is burnt the camera acquires mostly BB luminosity. Furthermore, this data shows that simple CH* chemiluminescence imaging in the 430 nm band mostly captures other species than CH* (Figure 8). Simultaneous imaging with a second camera in an adjacent wavelength band could be used to subtract the BB luminosity. Nevertheless, this would require precise calibration and possibly lead to noisy data.

The observed plateau value of OH* contribution in all variations might indicate that this spectral emission originates from the burnt zones with a similar composition. This would be in agreement with the OH* and CO_2* mechanisms, which predict persistent chemiluminescence from the hot burnt zones with the highest intensity at around stoichiometric conditions and a rapid drop of intensity at fuel richer/leaner conditions. The observed temporal evolution of the chemiluminescence emission is explained by this assumption as well, further confirmed by plotting the temporal evolution of the Abel-inverted OH* chemiluminescence images for a variation of ϕ_{CH4} (Figure 9). Abel inversion transforms the line-of-sight images to cross-section images based on the axial symmetry assumption. These images were obtained by ensemble-averaging over ten experimental repetitions followed by a Fourier-transform based inverse Abel-transformation method proposed by Pretzler [27]. Such transformation minimizes the noise common with the simpler Abel-inversion methods.

The diesel case (Figure 9, upper panels) after ignition shows a typical diesel lifted-flame two-branch OH* distribution [28]. The conditions at the spray axis are believed to be too rich to produce chemiluminescence. Some time after the end of injection (EOI) the two flame branches merge (image at 0.9 ms) as the EOI entrainment wave proceeds to reduce the pilot-fuel concentration upstream of the spray tip. At the spray tip, the mixture is still fuel-rich, thus resulting in a lower emission from the core of the spray. As the EOI entrainment further proceeds, the fuel-mixture continuously leans out leading to a recession of the OH* from upstream to the tip of the spray. This results in a horseshoe shape of the emission due to the spray-tip vortex.

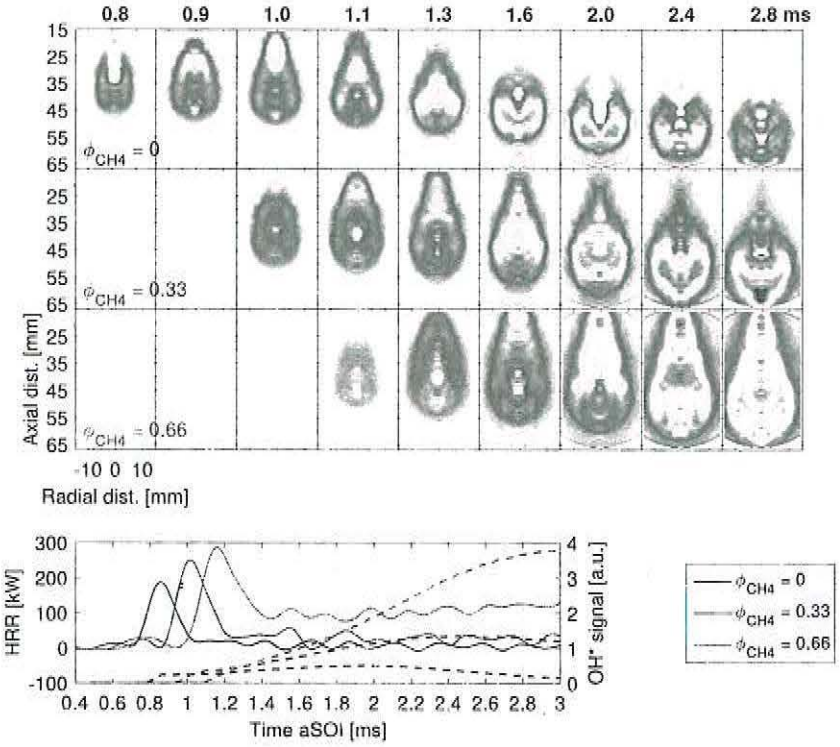

Figure 9: Temporal evolution of the Abel-inverted OH* images for variation of ϕ_{CH4}. Conditions: T_{SOI} = 850 K, ET = 400 µs. The bottom plot shows the evolution of the HRR (full line), and field-of-view integrated OH* imaging signal (dashed). Circles indicate the time instants of the image panels above.

The dual-fuel cases (Figure 9, middle and bottom rows) show a different evolution of the OH* emission. Due to the premixed methane, a longer persistence of the OH* emission in the wake of the spray is observed. Similarly, it also takes longer for the spray tip to lean-out. Overall, this results in large spray-plume volumes with close-to stoichiometric conditions, persisting long after the end-of-injection. This also explains the decoupled HRR rate and OH* emission (Figure 9, bottom plot). Premixed flame propagation is barely visible on OH* images due to the lean ϕ_{CH4} investigated in this study. Nevertheless, the overall heat release increases considerably due to the increased pilot-fuel quantity.

The findings imply a too low coupling between the OH* and HRR for any practical application. In other words, under dual-fuel engines conditions, the natural luminosity cannot be taken as a measure for the local HRR or HRR location as commonly done in HCCI/PCCI combustion [2,11]. Furthermore, the vast range of different signal intensities originating from different areas of the combustion chamber requires a high camera dynamic range to resolve both, the premixed and pilot-fuel regions. Under some conditions, light reflections from luminous premixed regions might exhibit higher intensities than the premixed flame propagation brightness.

5 Conclusions

The spectral footprint of diesel and dual-fuel combustion was investigated 1D-resolved along the injector axis using a spectrograph coupled to an intensified high-speed camera. In summary, the study revealed three primary chemiluminescence sources in both, diesel and dual-fuel combustion: OH*, CH* and broadband (BB) chemiluminescence. In the bandpass around 310 nm used for OH* imaging, about 60% of the luminosity originates from OH*. BB chemiluminescence (attributed mostly to CHO*, CH_2O*, and CO_2*) was identified as the source of the remaining signal. At late stages of combustion, the BB luminosity follows similar temporal and spatial evolution as OH*. Nevertheless, at early stages during the pilot-fuel burning

the temporal evolutions of OH* and BB chemiluminescence were different. In this stage, even the emission at 310 nm is dominated by the BB luminosity. Both emissions onset simultaneously at ignition and therefore do not interfere with the ignition delay detections. The emission of the CH* radical is a good tracer for the combustion of the pilot-fuel. However, due to the strong BB luminosity interference, it is challenging to detect CH* using bandpass-filtered imaging – an acquisition using a spectrograph might be required.

Based on the analysis of experimental data the following conclusions and implications for the evaluation of natural-luminosity images can be stated:

- OH*, CH* and BB luminosity show simultaneous onset at ignition and therefore equally qualify as a tracer for the determination of the ignition delay (ID). Integrated over the spectral domain the BB luminosity is the most intense. Furthermore, at ignition, the BB luminosity shows the steepest rise and can be therefore recommended for the future investigations of ID.
- The rise rate of luminosity at ignition decreases considerably with higher ϕ_{CH4} and with decreasing charge oxygen content. Large range of OH*/BB* intensity from ignition to late combustion stages poses a substantial problem due to the limited detector dynamic range and sensitivity. It is therefore imperative to use the lowest possible threshold when detecting ID based on OH*/BB* images in order to avoid over-prediction. If the sensitivity of the acquisition system is insufficient, the ignition delay might be considerably over-predicted.
- During the pilot-fuel burning, the light emission around 310 nm is dominated by the BB chemiluminescence. Therefore caution is needed when comparing the OH* temporal evolution with simulations considering OH* mechanism only.
- Commonly used CH* detection using 10 nm FWHM bandpass filter centered at 430 nm fails to distinguish the weak CH* emission from the broadband luminosity. Both, in the diesel and dual-fuel cases, less than 13% of the filtered light originates from CH*. Spectroscopic and/or two-wavelength detection would be needed to separate the CH* from the BB luminosity.
- Burned regions with close-to stoichiometric conditions dominate the flame emission at late stages of combustion. Especially at lean ϕ_{CH4} considerably more than an order of magnitude lower brightness is expected from the premixed flame regions. This explains the observed temporal evolution of OH* being decoupled from the HRR and poses a challenge for the detection of premixed burning zones.

Acknowledgements

Financial support from CCEM (project #803 "ScheDual") and the Swiss Federal Office of Energy (grant SI/501123-01) is gratefully acknowledged.

References

1. Pastor JV, García-Oliver JM, García A, Micó C, Durrett R (2013) A spectroscopy study of gasoline partially premixed compression ignition spark assisted combustion. Applied Energy 104:568-575. doi:http://dx.doi.org/10.1016/j.apenergy.2012.11.030
2. Najafabadi MI, Egelmeers L, Somers B, Deen N, Johansson B, Dam N (2017) The influence of charge stratification on the spectral signature of partially premixed combustion in a light-duty optical engine. Applied Physics B 123. doi:http://dx.doi.org/10.1007/s00340-017-6688-9
3. Hwang W, Dec J, Sjöberg M (2008) Spectroscopic and chemical-kinetic analysis of the phases of HCCI autoignition and combustion for single- and two-stage ignition fuels. Combustion and Flame 154 (3):387-409. doi:http://dx.doi.org/10.1016/j.combustflame.2008.03.019
4. Kim B, Kaneko M, Ikeda Y, Nakajima T (2002) Detailed spectral analysis of the process of HCCI combustion. Proceedings of the Combustion Institute 29 (1):671-677
5. Desantes JM, García-Oliver JM, Vera-Tudela W, López-Pintor D, Schneider B, Boulouchos K (2016) Study of the auto-ignition phenomenon of PRFs under HCCI conditions in a RCEM by means of spectroscopy. Applied Energy 179:389-400. doi:http://dx.doi.org/10.1016/j.apenergy.2016.06.134

6. Augusta R, Foster DE, Ghandhi JB, Eng J, Najt PM (2006) Chemiluminescence measurements of homogeneous charge compression ignition (HCCI) combustion. SAE Technical Paper 2006-01-1520. doi:https://doi.org/10.4271/2006-01-1520
7. Mancaruso E, Vaglieco BM (2011) Spectroscopic measurements of premixed combustion in diesel engine. Fuel 90 (2):511-520. doi:http://dx.doi.org/10.1016/j.fuel.2010.09.052
8. Mancaruso E, Vaglieco BM (2015) Spectroscopic analysis of the phases of premixed combustion in a compression ignition engine fuelled with diesel and ethanol. Applied Energy 143:164-175. doi:http://dx.doi.org/10.1016/j.apenergy.2015.01.031
9. Tang Q, Liu H, Yao M (2017) Simultaneous Measurement of Natural Flame Luminosity and Emission Spectra in a RCCI Engine under Different Fuel Stratification Degrees. SAE International Journal of Engines 10 (3). doi:10.4271/2017-01-0714
10. Bozkurt M, Fikri M, Schulz C (2012) Investigation of the kinetics of OH* and CH* chemiluminescence in hydrocarbon oxidation behind reflected shock waves. Applied Physics B 107 (3):515-527. doi:http://dx.doi.org/10.1007/s00340-012-5012-y
11. Sardeshmukh S, Bedard M, Anderson W (2017) The use of OH* and CH* as heat release markers in combustion dynamics. International Journal of Spray and Combustion Dynamics 9 (4):409-423. doi:http://dx.doi.org/10.1177/1756827717718483
12. Gaydon AG (1974) The Spectroscopy of Flames. Springer Netherlands, Dordrecht
13. Kopp M, Brower M, Mathieu O, Petersen E, Güthe F (2012) CO2 chemiluminescence study at low and elevated pressures. Applied Physics B 107 (3):529-538. doi:http://dx.doi.org/10.1007/s00340-012-5051-4
14. Kopp MM, Mathieu O, Petersen EL (2015) Rate Determination of the CO2 Chemiluminescence Reaction CO + O + M ⇄ CO2* + M: RATE DETERMINATION OF THE CO2* CHEMILUMINESCENCE REACTION. International Journal of Chemical Kinetics 47 (1):50-72. doi:http://dx.doi.org/10.1002/kin.20892
15. Hall JM, Petersen EL (2006) An optimized kinetics model for OH chemiluminescence at high temperatures and atmospheric pressures. International Journal of Chemical Kinetics 38 (12):714-724. doi:http://dx.doi.org/10.1002/kin.20196
16. Srna A, Bolla M, Wright YM, Herrmann K, Bombach R, Pandurangi SS, Boulouchos K, Bruneaux G (2018) Effect of methane on pilot-fuel auto-ignition in dual-fuel engines. Proceedings of the Combustion Institute 37. doi:http://dx.doi.org/10.1016/j.proci.2018.06.177
17. Srna A, Bruneaux G, von Rotz B, Bombach R, Herrmann K, Boulouchos K (2018) Optical Investigation of Sooting Propensity of n-Dodecane Pilot/Lean-Premixed Methane Dual-Fuel Combustion in a Rapid Compression-Expansion Machine. SAE Technical Paper 2018-01-0258. doi:http://dx.doi.org/10.4271/2018-01-0258
18. Schlatter S, Schneider B, Wright YM, Boulouchos K (2013) Comparative Study of Ignition Systems for Lean Burn Gas Engines in an Optically Accessible Rapid Compression Expansion Machine. SAE Technical Paper 2013-24-0112. doi:http://dx.doi.org/10.4271/2013-24-0112
19. Schlatter S, Schneider B, Wright YM, Boulouchos K (2016) N-heptane micro pilot assisted methane combustion in a Rapid Compression Expansion Machine. Fuel 179:339-352. doi:http://dx.doi.org/10.1016/j.fuel.2016.03.006
20. Rochussen J, Kirchen P (2018) Characterization of reaction zone growth in an optically accessible heavy-duty diesel/methane dual-fuel engine. International Journal of Engine Research:In press, 2019. doi:http://dx.doi.org/10.1177/1468087418756538
21. Ahmad Z, Aryal J, Ranta O, Kaario O, Vuorinen V, Larmi M (2018) An Optical Characterization of Dual-Fuel Combustion in a Heavy-Duty Diesel Engine. SAE Technical Paper 2018-01-0252. doi:http://dx.doi.org/10.4271/2018-01-0252
22. Skeen SA, Manin J, Pickett LM (2015) Simultaneous formaldehyde PLIF and high-speed schlieren imaging for ignition visualization in high-pressure spray flames. Proceedings of the Combustion Institute 35:3167-3174. doi:http://dx.doi.org/10.1016/j.proci.2014.06.040
23. Kammermann T, Koch J, Wright YM, Soltic P, Boulouchos K (2017) Generation of Turbulence in a RCEM towards Engine Relevant Conditions for Premixed Combustion Based on CFD and PIV Investigations. SAE International Journal of Engines 10 (4). doi:http://dx.doi.org/10.4271/2017-24-0043
24. Schlatter S, Schneider B, Wright Y, Boulouchos K (2012) Experimental Study of Ignition and Combustion Characteristics of a Diesel Pilot Spray in a Lean Premixed Methane/Air Charge using a Rapid Compression Expansion Machine. SAE Technical Paper 2012-01-0825. doi:http://dx.doi.org/10.4271/2012-01-0825
25. Musculus MPB (2005) Measurements of the Influence of Soot Radiation on In-Cylinder Temperatures and Exhaust NOx in a Heavy-Duty DI Diesel Engine. SAE Technical Paper 2005-01-0925. doi:http://dx.doi.org/10.4271/2005-01-0925
26. Iijima A, Shoji H (2007) A Study of HCCI Combustion Characteristics Using Spectroscopic Techniques. SAE Technical Paper 2007-01-1886. doi:10.4271/2007-01-1886
27. Pretzler G (1991) A New Method for Numerical Abel-Inversion. Zeitschrift fur Naturforschung - Section A Journal of Physical Sciences 46 (7):639-641. doi:http://dx.doi.org/10.1515/zna-1991-0715
28. Maes N, Meijer M, Dam N, Somers B, Baya Toda H, Bruneaux G, Skeen SA, Pickett LM, Manin J (2016) Characterization of Spray A flame structure for parametric variations in ECN constant-volume vessels using chemiluminescence and laser-induced fluorescence. Combustion and Flame 174:138-151. doi:http://dx.doi.org/10.1016/j.combustflame.2016.09.005